A new approach to the design of a speed–torque-controlled rubber V-belt variator

M Cammalleri
Università di Palermo, Dipartimento di Meccanica, Viale delle Scienze, Palermo, 90128, Italy.
email: cammalleri@dima.unipa.it

The manuscript was received on 8 September 2004 and was accepted after revision for publication on 17 August 2005.

DOI: 10.1243/095440705X35080

Abstract: This paper presents a new model for a torque–speed-sensing rubber V-belt variator. The actuators are of the centrifugal roller kind on the driver side and a helical torque cam plus a compression–torsion spring on the driven side. The equations permit designing the actuator geometry in order to keep the transmissible torque as close as possible to the torque request in the whole operative field.

Moreover, a procedure is suggested for the most proper design of an automatic variator of this kind. It permits choosing the required variogram of the transmission, i.e. the matching between the engine and the transmission, and designing the actuators: roller mass, housing shape, contact plate angle for the centrifugal roller actuator, and helical guide slope for the torque cam actuator. Furthermore, the degree of engine transmission matching can be calculated at part load for fixed actuators.

Extensive experimental tests were carried out on a proper bench test to validate the procedure.

Keywords: continuously variable transmission, rubber V-belt, automatic transmission, axial thrusts regulation

1 INTRODUCTION

Continuously variable transmissions (CVTs) are successfully applied at present in many mechanical systems in order to improve the overall performances. In low-power vehicles, such as scooters, rubber V-belt CVTs of the expanding pulley type are widely used. In fact, the power can be transmitted by a rubber V-belt variator under relatively low axial thrust, owing to the high coefficient of friction of the rubber, which enables transmission control to be attained by pure mechanical actuators with no need for external power.

Furthermore, it is possible to modify the characteristics of a CVT, e.g. the aperture (the ratio of the maximum speed ratio to the minimum speed ratio), the transmissible power or the efficiency, by using split-way drives with two parallel lines, one with a variable speed and the other with a fixed ratio. These combinations offer very interesting chances as regards the realization of self-regulating drives. Also, it has to be pointed out that a double-way drive implies different boundary conditions for the CVT unit with respect to the simple method, when varying the speed ratio at given input torque and speed [**1**, **2**].

In this paper, new equations for the actuator axial thrust in an automatic variator are derived. The aim is to choose the actuator geometry so that the transmissible torque is kept as close as possible to the required torque in the whole operative field.

In general a pulley consists of two flanges with a conical shape; one of these is axially fixed and the other is movable. The axial motion of the movable flange is produced by the unbalance between the thrust of the belt in the groove on one side and of the actuator on the other side.

In a scooter variator in particular, the driver pulley actuator consists of centrifugal rollers pushing against curved ramps; the result is a speed-sensing pulley where the rotational speed increase causes the outward motion of the V-belt. The driven pulley actuator consists of a helical compression spring and of a number of helical guides which convert the output torque into an axial force increase; the result is a torque-sensing pulley where the output torque increase forces the movable half-pulley to close and thereby the pitch diameter to increase. These components act together and, at equilibrium, all forces and torques are balanced and dictate a particular operative point. The result is an automatic transmission which adjusts itself to any change in the input speed and in the output torque.

Therefore, it is clear that, in order to estimate the overall variator performance, it is necessary to investigate thoroughly the mechanical behaviour of the control actuators as well as of the V-belt.

Previously Oliver *et al.* [**3**], followed by other workers [**4**, **5**], formulated some models for the axial thrusts, for fixed geometry of the actuators. However, none of these is applicable to the reverse case, i.e. to finding the actuator geometry for a fixed axial thrust. In fact, all these models assume constant curvature radii of the ramps and constant slope of the helical guides.

As regards rubber V-belt mechanics, Gerbert [**6**] developed an extensive and deep analysis, which requires, however, numerical procedures that are too elaborate for the calculation of the axial thrusts. Therefore, for practical design purposes, approximate formulae have generally been used up to now [**7**, **8**]. In this paper, new equations for the thrust of the actuators are derived, using recent closed-form solutions for rubber V-belts mechanics [**9**].

Moreover, a new approach to the most proper design of this type of variator is suggested. It permits choosing the variogram of the transmission, i.e. the desired matching between the engine and the transmission, and designing the actuators: roller mass, housing shape, contact plate angle for the centrifugal actuator, and helical slope for the torque cam actuator. Furthermore, the degree of engine transmission matching can be calculated at part load for fixed actuator.

Extensive experimental tests were carried out on a proper bench test to validate the procedure.

2 VARIOGRAM

The variogram of a CVT transmission is the diagram that describes the mutual dependence between the output and input speeds and, thus, it correlates in practice the speed ratio with the motor speed. A typical CVT variogram is shown in Fig. 1 in normalized coordinates (i.e. scaled by their respective maximum values).

For a given drive aperture, all points lying between the lower and upper straight lines, which refer to the minimum and maximum speed ratios respectively, could be possible operative points in theory. Nevertheless, this working freedom would require a control system for the speed ratio independent of the applied torque; this is what actually happens in the case of industrial variators. Considering a self-regulating CVT for vehicle application on the contrary and assuming full load from the prime motor, the speed ratio remains constant and minimum as far as a certain input angular speed n_{axi} and then starts to increase until it reaches its top value. The curve in Fig. 1 implies a relationship between the speed ratio and the motor angular speed, $n_{\mathrm{a}} = n_{\mathrm{a}}(\tau_{\mathrm{v}})$, which is able to be represented, for example, for $n_{\mathrm{ax}} \geqslant n_{\mathrm{axi}}$ by the equation

$$n_{\mathrm{a}x} = 1 - \frac{1 - \tau/\tau_{\mathrm{M}}}{\tau/\tau_{\mathrm{m}} - \tau/\tau_{\mathrm{M}}}(1 - n_{\mathrm{axi}}) \tag{1}$$

3 MOTOR

It is assumed that the engine torque depends on the angular speed $c_{\mathrm{a}} = c_{\mathrm{a}}(n_{\mathrm{a}})$, as in Fig. 2, which is typical of an internal combustion engine, according to

$$\begin{aligned} c_{\mathrm{a}x} &= 2n_{\mathrm{axcOT}}n_{\mathrm{a}x} + (\mathrm{OT} - n_{\mathrm{axc}}^2) - n_{\mathrm{a}x}^2 \\ n_{\mathrm{axcOT}} &= n_{\mathrm{axc}} - (1 - \mathrm{OT})(n_{\mathrm{axc}} - n_{\mathrm{axmin}}) \end{aligned} \tag{2}$$

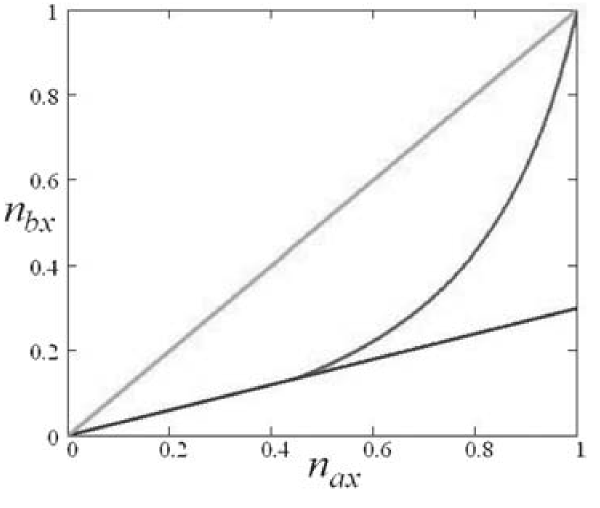

Fig. 1 CVT variogram

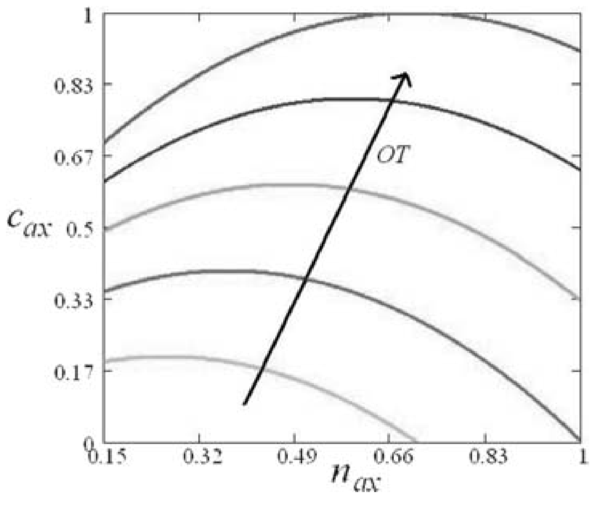

Fig. 2 Characteristic curves of an internal combustion engine

where c_{ax} and n_{ax} are the normalized torque and angular speed respectively, OT ($=0$–1) is the throttle opening degree, n_{axc} is the angular speed of maximum torque at wide-open throttle (WOT) (i.e. OT $=1$), and n_{axmin} is the idling angular speed.

4 VARIATOR

4.1 Variator geometrical parameters

Figure 3 defines the main mechanical and geometrical quantities of the variator. The subscripts a and b refer to the primary and secondary pulleys respectively. Fixing the variator speed ratio, τ_v, all the other quantities are uniquely determined. The wrap radii R_a and R_b over the two pulleys are given by the constancy of the belt length $L=(\pi+2\beta_v)R_a+(\pi-2\beta_v)R_b+2h\cos\beta_v$, where $\beta_v=\arcsin[(R_a-R_b)/h]$. The wrap angles are $\theta_a=\pi+2\beta_v$ and $\theta_b=\pi-2\beta_v$. Finally the axial displacements of the two movable half-pulleys are $\Delta x_a=2\tan\alpha(R_a-R_{am})$ and $\Delta x_b=2\tan\alpha(R_{bM}-R_b)$.

4.2 V-belt mechanics

Applying the Euler–Grashof theory to the V-belt leads to a relationship for the axial thrust in the form $F_z=(T_1-qV^2)Z(\theta_s,\tau_v)$, where T_1 is the tight-side belt tension, q and V are the belt mass per unit length and the belt speed respectively, while $Z(\theta_s,\tau_v)$ is a specific function of the speed ratio τ_v and of the slip angle θ_s [**1**]. Nevertheless it is well known that the belt elastic penetration into the groove due to the side compression of the pulley walls and the consequent radial components of the frictional forces play an important role in the V-belts mechanics [**6**, **10**]. Considering this effect, however, the above expression of the axial thrust may be kept unchanged, except that a different functional dependence $Z(\theta_s,\tau_v)$, has to be imposed, where the θ_s values are different in general for the two pulleys (in practice, $\theta_{sa}\leqslant\theta_{sb}$), in accordance with the different force distributions along the arcs of contact. Summing up, the variator

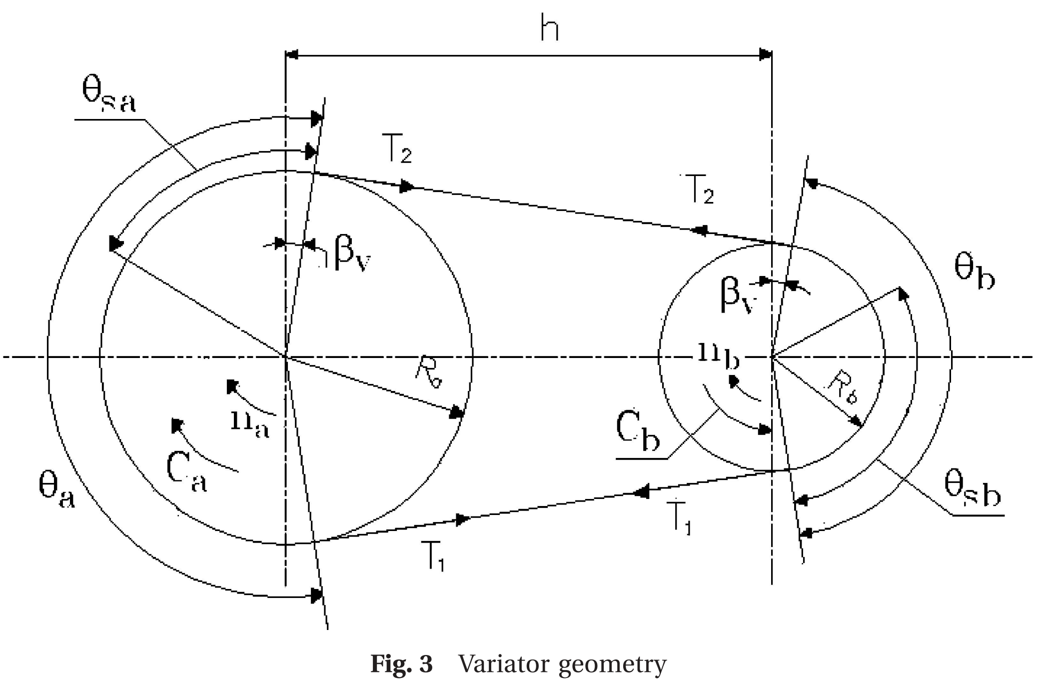

Fig. 3 Variator geometry

equilibrium gives

Driver pulley		Driven pulley
$C_a = (T_1 - T_2)R_a$	Rotational equilibrium	$C_b = (T_1 - T_2)R_b$
$\dfrac{T_2 - qV^2}{T_1 - qV^2} = G_a(\theta_{sa}, \tau_v)$	Belt equilibrium (tension distribution)	$\dfrac{T_1 - qV^2}{T_2 - qV^2} = G_b(\theta_{sb}, \tau_v)$
$F_{za} = \dfrac{T_1 - qV^2}{2\tan(\alpha + \varphi)} \times Z_a(\theta_{sa}, \tau_v)$	Axial equilibrium (axial forces)	$F_{zb} = \dfrac{T_2 - qV^2}{2\tan(\alpha + \varphi)} \times Z_b(\theta_{sb}, \tau_v)$

where φ is the angle of sliding friction between the belt and the pulley. The mechanical behaviour of the variator is governed by the equilibrium conditions, which consist of the previous set of six equations in the ten variables n_a, C_a, θ_{sa}, F_{za}, T_1, T_2, τ_v, C_b, θ_{sb}, and F_{zb} ($V \propto n_a$). Thus, four variables could be chosen arbitrarily to control the variator.

Nevertheless, for given actuators, the axial forces F_{za} and F_{zb} on the half-pulleys are no longer independent variables and, thus, the dependences of the steady state speed ratio τ_v on the driving angular speed n_a and on the output torque C_b, for example, are uniquely determined.

In the course of a design stage, on the contrary, the choice may be made to impose the drive variogram [equation (1)] $n_a = n_a(\tau_v)$, the WOT torque curve [equation (2)] $C_a = C_a(n_a)$ and therefore $C_b = C_b(\tau_v)$, and the belt adhesion limit (which means the minimization of the belt maximum tension $\theta_{sb} = \sigma\theta_b(\tau_v)$, where $\sigma < 1$ is a safety factor). In this manner, it is then possible to determine the dependence of the axial forces of the belt on the pulleys on the speed ratio τ_v and to use them as entries for the actuator design according to

$$F_{zb} = \frac{C_b}{R_b 2\tan(\alpha + \varphi)} \frac{Z_b(\theta_{sb}, \tau_v)}{G_b(\theta_{sb}, \tau_v) - 1} \tag{3}$$

$$F_{zb} = \frac{C_b}{R_b 2\tan(\alpha + \varphi)} \frac{Z_b(\theta_{sb}, \tau_v)}{G_b(\theta_{sb}, \tau_v) - 1} \tag{4}$$

The functions G and Z are obtainable by integration of a differential system including the equilibrium conditions in the direction parallel and normal to the belt and other geometric and kinematic conditions [**6**, **10**]. Unfortunately, such an integration can be carried out only by complex numerical procedures and many efforts have been made in the past by some workers in order to formulate simpler approximate solutions for quicker calculations [**7**, **8**]. Sorge *et al.* [**9**] have recently proposed closed-form solutions, applicable to those belts that are much stiffer in the longitudinal than in the transverse direction. The solutions proposed in reference [**9**] are somehow more complex than those in references [**7**] and [**8**] but provide results almost identical with those obtainable by the Runge–Kutta numerical integration of Gerbert's [**6**] model, which is recognized as the most accurate model worldwide for rubber V-belt mechanics. Therefore those solutions, briefly reported in appendix 2, are here applied.

Equations (3) and (4) are valid for an ideal V-belt. In practice the output torque C_b must be divided by the square root of the torque efficiency η_t (assuming equal torque losses for both pulleys) and the geometrical wrap angles θ_a and θ_b of the previous section have to be reduced, owing to the elastic flexural stiffness S_f of the belt [**6**], replacing

$$\begin{aligned} \theta_a &\to \theta_a - \frac{\sqrt{S_f}}{R_a}\left(\frac{1}{\sqrt{T_1 - qV^2}} + \frac{1}{\sqrt{T_2 - qV^2}}\right) \\ \theta_b &\to \theta_b - \frac{\sqrt{S_f}}{R_b}\left(\frac{1}{\sqrt{T_1 - qV^2}} + \frac{1}{\sqrt{T_2 - qV^2}}\right) \end{aligned} \tag{5}$$

The flexural stiffness S_f was obtained experimentally as described in appendix 3.

4.3 Primary actuator

The centrifugal mass regulator consists of an axially fixed plane ramp and a curved ramp moving with the movable half-pulley. A number of rollers are located in the space between the two ramps. They rotate together with the pulley and, owing to the centrifugal force, push the plates away from each other, varying the speed ratio (Fig. 4).

Oliver *et al.* [**3**], followed by other workers [**4**, **5**], have proposed some formulae for the calculation of the axial forces for given geometry of the actuator. Nevertheless, these models are not suited for inverse use, i.e. to obtain the ramp profiles for given axial forces, since they are based on the hypothesis that the curved ramp is a circular arc. On the contrary, the present model permits defining the centrifugal actuator geometry completely for a given law of variation in the axial thrust, or else calculating the axial thrust for a given ramp profile of any shape.

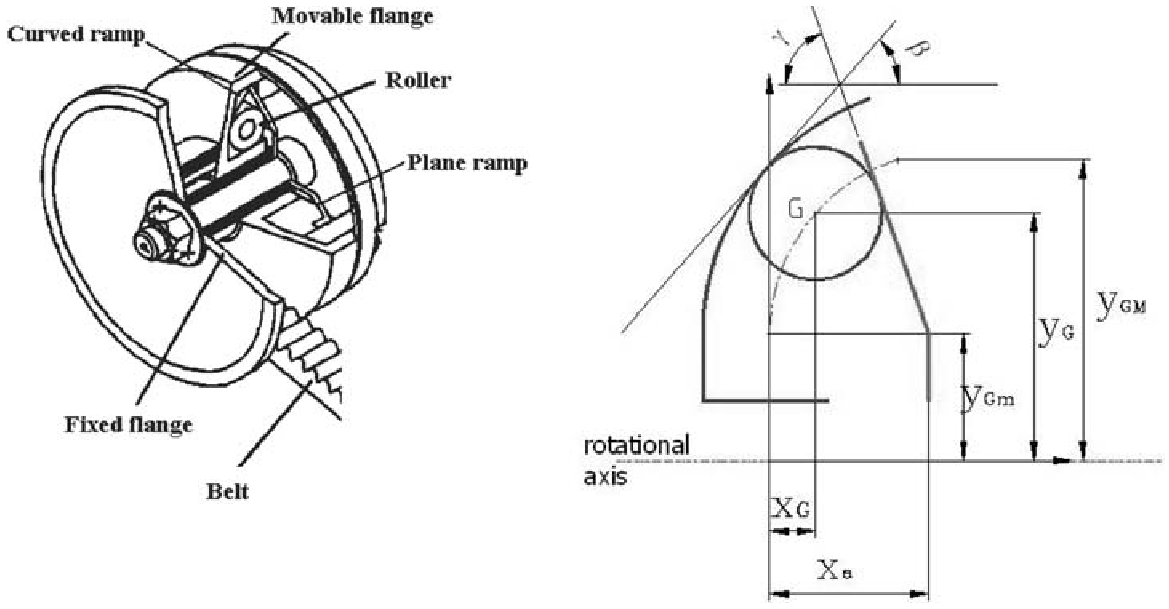

Fig. 4 Centrifugal mass regulator

4.3.1 Roller equilibrium and axial thrust

Figure 5 shows the roller free-body diagram on the hypothesis of incipient upshift (increase in the speed ratio). Imposing radial, axial, and rotational equilibrium, it is possible to write

$$\uparrow \quad F_{\text{cen}} = F_{\text{d}x} \cos(\gamma - \varphi_{\text{d}x}) + F_{\text{s}x} \cos(\beta - \varphi_{\text{s}x})$$

$$\leftarrow \quad F_{\text{d}x} \sin(\gamma - \varphi_{\text{d}x}) = F_{\text{s}x} \sin(\beta - \varphi_{\text{s}x})$$

$$\circlearrowleft \quad F_{\text{d}x} \sin(\varphi_{\text{d}x}) = F_{\text{s}x} \sin(\varphi_{\text{s}x})$$

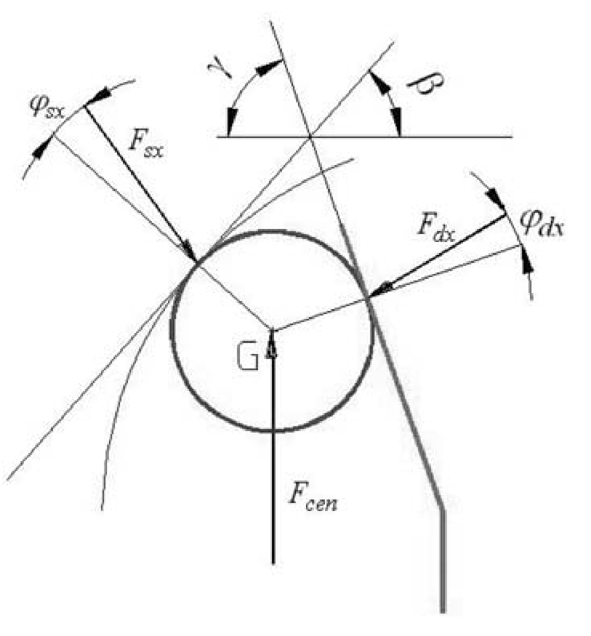

Fig. 5 Free-body diagram of the roller

Since $F_{\text{zacta}} = F_{\text{d}x} \sin(\beta - \varphi_{\text{s}x})$ and $F_{\text{cen}} = Mn_{\text{a}}^2 y_{\text{G}}$, the first two equations give the axial force produced by the centrifugal actuator according to

$$F_{\text{zacta}} = \frac{Mn_{\text{a}}^2 y_{\text{G}}}{\cot(\gamma - \varphi_{\text{d}x}) + \cot(\beta - \varphi_{\text{s}x})} = F_{\text{zacta}}(\tau_{\text{v}}, n_{\text{a}}) \tag{6}$$

where M is the total mass of the rollers, y_{G} is the distance of their mass centre G from the pulley axis, and β is the angle formed by the pulley axis and the tangent to the curved profile at the contact point, parallel to the trajectory of G (Fig. 4). Combining the second and third equations, some information on the roller motion is obtainable and is given by

$$\frac{\sin(\gamma - \varphi_{\text{d}x})}{\sin(\varphi_{\text{d}x})} = \frac{\sin(\beta - \varphi_{\text{s}x})}{\sin(\varphi_{\text{s}x})} \tag{7}$$

It is possible to deduce that, for $\beta > \gamma$, $\varphi_{\text{s}x} = \varphi_{\text{a}} > \varphi_{\text{d}x}$ [$\varphi_{\text{d}x}$ from equation (7)] and the roller rolls on the right ramp and slips on the left ramp while, for $\beta < \gamma$, $\varphi_{\text{s}x} < \varphi_{\text{d}x} = \varphi_{\text{a}}$ [$\varphi_{\text{s}x}$ from equation (7)] and the roller rolls on the left ramp and slips on the right ramp (here φ_{a} is the angle of sliding friction between the roller and the ramp).

In the condition of incipient downshift, the frictional forces reverse their directions and the angles $\varphi_{\text{d}x}$ and $\varphi_{\text{s}x}$ change their sign in the above relationships, but all the conclusions on the roller motion remain the same.

4.4 Secondary actuator

The axial thrust needed to ensure the adherence between the belt and the pulley is usually produced by a helical spring compressed between the secondary movable half-pulley and a fixed contrast wall. Moreover, in motorcycle variators, an additional thrust proportional to the output torque is generated by sloping the sliding guides of a certain angle δ (constant in Fig. 6).

The axial equilibrium of the movable half-pulley yields

$$F_{\mathrm{zactb}} = (F_0 + K\Delta x_{\mathrm{b}}) + \frac{C_{\mathrm{b}}}{d}\tan(\delta \pm \varphi_{\mathrm{b}}) = F_{\mathrm{zactb}}(\tau_{\mathrm{v}}, C_{\mathrm{b}}) \tag{8}$$

where F_0 and K are the pre-load and the stiffness of the helical spring respectively, d is the mean diameter of the helical guide, and $\pm\varphi_{\mathrm{b}}$ is the angle of friction of the guide in case of incipient upshift or downshift respectively.

Depending on the spring constraints, the half-pulley displacement may cause some torsion of the spring. In this case the reaction torque yields an additional axial thrust, which is a function of the transmission ratio. Summing up, the expression for the actuator axial thrust remains the same provided that the spring stiffness

$$K_{\mathrm{eq}} = \left[1 + (1+\nu)\left(D\frac{\tan\delta}{d}\right)^2\right]K$$

is used in place of K, where v and D are Poisson's ratio and the mean diameter of the spring respectively.

5 INVERSE ANALYSIS

5.1 Roller housing determination

Assuming a coordinate reference as in Fig. 4, in motion with movable half-pulley, it is possible to write for a generic position of the roller

$$x_{\mathrm{a}} = x_{\mathrm{G}} + r\sin\gamma + \cot\gamma\,(y_{\mathrm{G}} - y_{\mathrm{Gm}} + r\cos\gamma)$$

$$\frac{\mathrm{d}y_{\mathrm{G}}}{\mathrm{d}x_{\mathrm{G}}} = \tan\beta$$

and hence

$$\frac{\mathrm{d}x_{\mathrm{a}}}{\mathrm{d}y_{\mathrm{G}}} = \cot\gamma + \cot\beta$$

where $\mathrm{d}x_{\mathrm{a}} = 2\,\mathrm{d}R_{\mathrm{a}}\tan\alpha$. As $F_{z\mathrm{acta}} = F_{z\mathrm{a}}$ at equilibrium, neglecting the friction, equation (6) gives

$$y_{\mathrm{G}}\,\mathrm{d}y_{\mathrm{G}} = \frac{2\tan\alpha}{Mn_{\mathrm{a}}^2}F_{z\mathrm{a}}\,\mathrm{d}R_{\mathrm{a}} \tag{9}$$

which is the differential equation of the trajectory of G on varying τ_{v}. Note that equation (9) expresses the principle of virtual displacements.

Integrating equation (9) gives

$$y_{\mathrm{G}} = \sqrt{\frac{4\tan\alpha}{M}I(\tau_{\mathrm{v}}) + y_{\mathrm{Gm}}^2} \tag{10}$$

where $I(\tau_{\mathrm{v}}) = \int_{\tau_{\mathrm{vm}}}^{\tau_{\mathrm{v}}} (F_{z\mathrm{a}}/n_{\mathrm{a}}^2) \times (\mathrm{d}R_{\mathrm{a}}/\mathrm{d}\tau_{\mathrm{v}})\,\mathrm{d}\tau_{\mathrm{v}}$.

Fixing y_{GM} and y_{Gm}, e.g. by their dependences on the pulley size and on the primary shaft diameter, it is possible to calculate the total mass needed for the

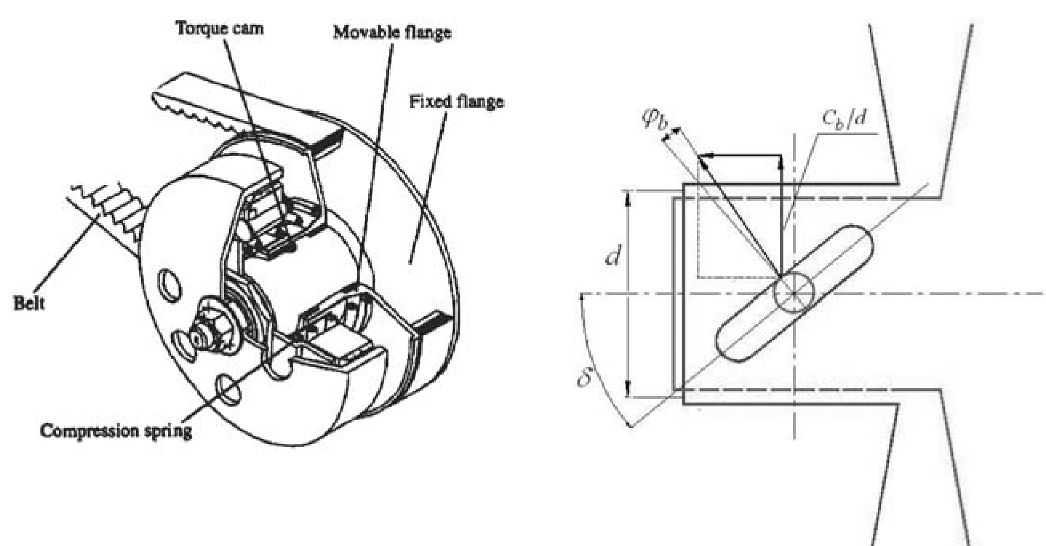

Fig. 6 Secondary actuator

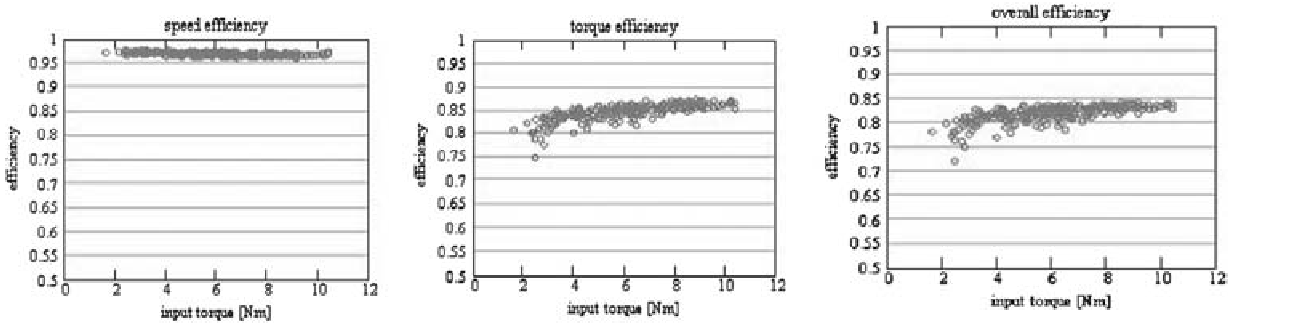

Fig. 7 Experimental variator efficiency

rollers from

$$M = \frac{4 \tan \alpha \, I(\tau_{vM})}{y_{Gm}^2 - y_{Gm}^2} \tag{11}$$

Since $\tan \beta$ must be not less than zero, equation (6) gives

$$\tan \gamma \geqslant \frac{dy_G}{dx_a} = \frac{F_{za}}{Mn_a^2 y_G} \tag{12}$$

which can be used to choose a value for γ. Then the trajectory of the roller centre G is given by

$$x_G(\tau_v) = \Delta x_a - \frac{y_G - y_{Gm}}{\tan \gamma} \tag{13}$$

and simple geometrical consideration yields the curved ramp profile

$$x_p = x_G - r \sin \beta, \qquad y_p = y_G + r \cos \beta \tag{14}$$

where x_p and y_p are the ramp profile coordinates in the reference system of Fig. 4.

5.2 Cam slope determination

Since equilibrium requires $F_{zactb} = F_{zb}$, neglecting the friction in the guides, it is possible to obtain

$$\tan \delta = [F_{zb} - (F_0 + K \Delta x_b)] \frac{d}{C_b} \tag{15}$$

which is the differential equation of the guide line. F_0 and K can be calculated by imposing boundary values for the angle δ at τ_{vm} and τ_{vM} respectively. Sometimes it is possible to choose F_0 and K so that δ turns out to be nearly constant.

5.3 An example case

The data in Table 1 are used for the variator geometry and the belt properties. A constant efficiency is assumed for simplicity (this is approximately true for medium–high load, see experimental data in Fig. 7). Moreover, putting $n_{axi} = 0.65$ into equation (1) of

Table 1 Variator and belt data

Variator		Belt	
Parameter	Value	Parameter	Value
τ_{vm}	0.313	k_0	0.15
τ_{vM}	1.298	f	0.48
L	770 mm	η_s	0.96
h	255 mm	η_t	0.85
α	12.8°	S_f	10 kN mm^2
		q	0.124 kg/m

the variogram and $n_{axc} = 0.75$, $n_{axmin} = 0.33$, $C_{amax} = 3.2$ N m, and $n_{amax} = 9000$ r/min (typical of a 50 cm^3 engine) into equation (2) of the motor, $\theta_{sb} = 0.8\theta_b(\tau_v)$ into equation (3) of the variator, it is found that $M = 0.0208$ kg from equation (11) of the primary actuator. Then equations (10) and (13) give the roller centre's trajectory, and equation (15) the curved ramp profile (Fig. 8). Finally, assuming that $F_0 = 95$ N and $K = 1.56$ N/mm, equation (4) of the variator and equation (15) of the secondary actuator give the helical cam angle on varying τ_v (Fig. 9).

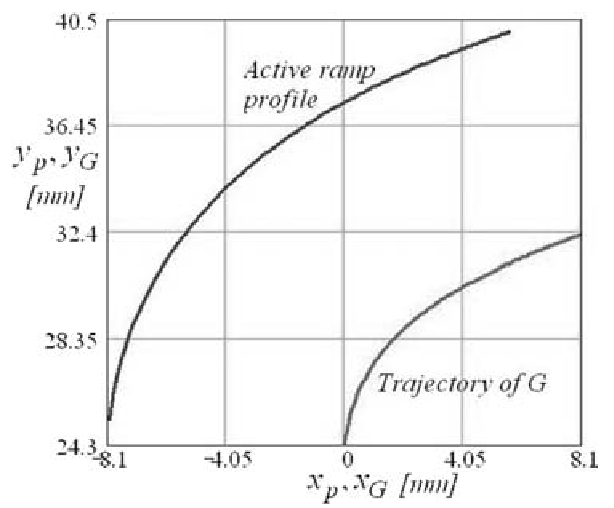

Fig. 8 Curved profile and roller centre trajectory

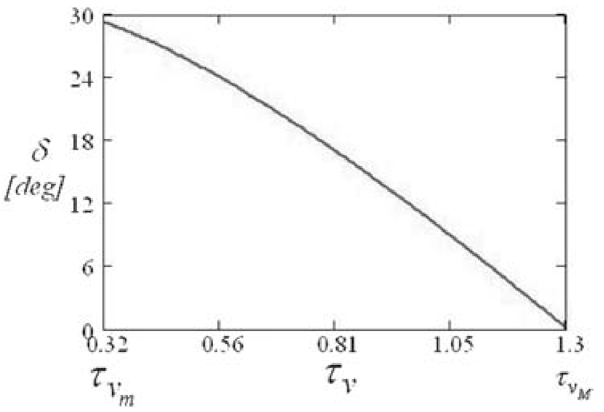

Fig. 9 Helical cam angle δ

6 DIRECT ANALYSIS

When the geometry of each actuator is given, the equilibrium conditions of section 4.2 allow analysis of the drive behaviour in any condition. In fact, comparing equations (6) and equation (3), and equations (8) and (4), two equations in the four variables n_a, τ_v, C_b, and θ_s are obtained as

$$\frac{Mn_a^2 y_G(\tau_v)}{\cot\beta(\tau_v)+\cot\gamma} = \frac{C_b}{2\tan(\alpha+\varphi)\,R_b(\tau_v)}\,\frac{G_b(\theta_{sb},\tau_v)}{G_b(\theta_{sb},\tau_v)-1}\,\theta_a(\tau_v)$$

$$F_0+K\Delta x_b(\tau_v)+C_b\frac{\tan\delta(\tau_v)}{d} = \frac{C_b}{2\tan(\alpha+\varphi)\,R_b(\tau_v)}\,\frac{Z_b(\theta_{sb},\tau_v)}{G_b(\theta_{sb},\tau_v)-1} \quad (16)$$

Calculating θ_{sb} from the first equation and replacing it into the second give the relationship

$$\mathrm{VOM}(\tau_v, n_a, C_b)=0 \quad (17)$$

where VOM represents the variator operative map in the three-dimensional space (τ_v, n_a, C_b).

On the other hand, if the variator is driven by an internal combustion engine, another relationship between the input angular speed n_a and the input torque C_a (see Fig. 2) must be added and therefore, accounting for torque efficiency η_t and the speed ratio τ_v, between n_a and the output torque C_b. Consequently equation (17) becomes a relationship between τ_v and n_a, i.e. the drive variogram, which therefore turns out to be uniquely determined. At part load, the relation between n_a and C_a is different from the case of WOT and the variogram is different.

For example, using the data in Table 1 (see section 5.3) for the variator and the data in Table 2 (see section 7.1) for the actuators, by use of a trial-and-error procedure with very fast convergence, equation (17) gives the diagram in Fig. 10.

Assuming an engine like the previous engine, the variograms in Fig. 11 can be obtained on varying the OT.

7 EXPERIMENTAL VERIFICATION

7.1 Evaluation of the variator parameters

Extensive experimental tests were carried out on a suitable bench test to validate the analysis.

First of all, the actuator parameters of a commercial scooter variator were measured (Table 1 and Table 2). In order to outline the exact shape of the centrifugal actuator ramps, some wax was fused in the roller housing, the mould was digitalized by a high-resolution scanner, and the image was processed. The result of this analysis was an *x–y* matrix representing the curved ramp profile (Fig. 12). The rollers were weighed by a precision balance and

Table 2 Actuator data

Primary actuator		Secondary actuator	
Parameter	Value	Parameter	Value
r	8.1 mm	F_0	275 N
y_{Gm}	15.2 mm + r	K_{eq}	10.6 N/mm
M	56.1 gr	d	38.5 mm
x_p, y_p	Fig. 12	δ	38°
γ	66.5°		

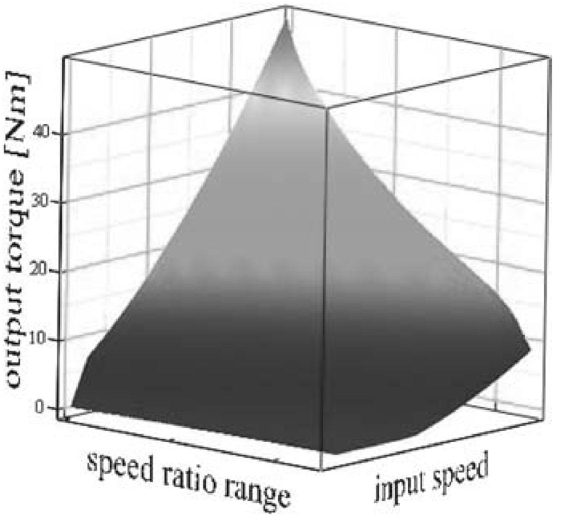

Fig. 10 VOM, with the input speed range from 5500 to 11 500 r/min

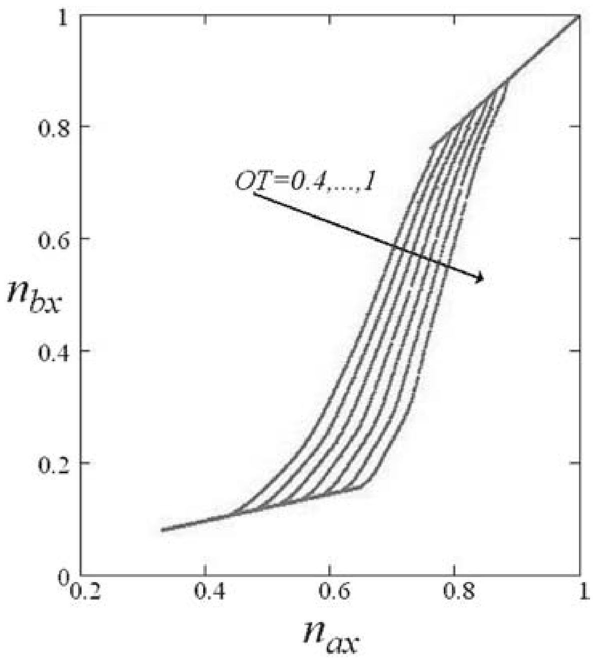

Fig. 11 Variograms at several part loads

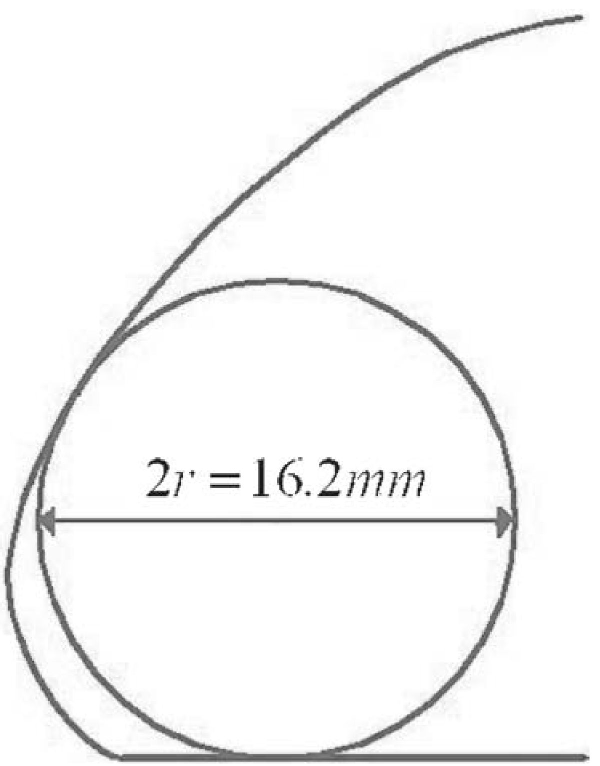

Fig. 12 Experimental curved ramp

the spring stiffness was calculated through a load–displacement diagram obtained by a test machine. The helical cam slope was constant. All the other geometrical dimensions were taken by a vernier caliper. All the angles were derived by Pythagoras' theorem.

7.2 Test rig

With reference to Figs 13 and 14, a d.c. electric motor 1 drove the transmission, and a disc brake 7, which was pneumatically operated, exerted the output torque. The variator 5 was of the small-size high-speed type with a maximum power of about 17 kW at 10 800 r/min. Owing to the lower speed restriction of the d.c. electric motor, two gear couplings were connected upstream 4 and downstream 6 of the variator, stepping the speed up and down respectively with ratios reciprocal to each other and permitting a sufficient power level to be delivered through the variable-speed unit.

The driver and driven speeds and torques were measured by two speed–torque meters 2 of the strain-gauge type while the belt pitch radii were measured by two laser displacement sensors 3. The temperature of the oil in the gearboxes was recorded by two thermocouples.

All signals were conveyed to a data acquisition system and analysed by a proper routine.

The power losses in the gears 4 and 5 depend almost only on the working speed. They were taken into consideration in the evaluation of the driver and driven torques inside the variator, which is considered as a single unit without the end gears.

The torque directly applied to the inside driver pulley is $C_a = (C_1 - C_{10})/13$, where C_1 is the torque of the input torque-meter, 13 is the gear speed ratio, and C_{10} is the torque lost in the upstream gearing. Similarly, the torque directly applied to the inside driven pulley is $C_b = (C_2 + C_{20})/13$. The torques C_{10} and C_{20} were measured by experiments at several angular speeds, taking away the belt. For an angular speed range of the speed-meters from 450 to 750 r/min, the torques C_{10} and C_{20} lost in the upstream gearing came out to be nearly constant and both equal to 2 N m.

7.3 Experiment

The entire variator speed ratio range was covered, keeping the input angular speed constant and increasing the output torque, or vice versa. The measurements were stored when all sensor signals were stabilized. The data were from 2 to 15 N m for the output torque and from 5000 to 9000 r/min for the input angular speed. The total number of test points was 272.

Unfortunately, the load from the disc brake was not exactly constant. It was therefore impossible to specify whether the drive was in an impending upshift or downshift at the storing moment. Thus, it was also impossible to know the exact direction of

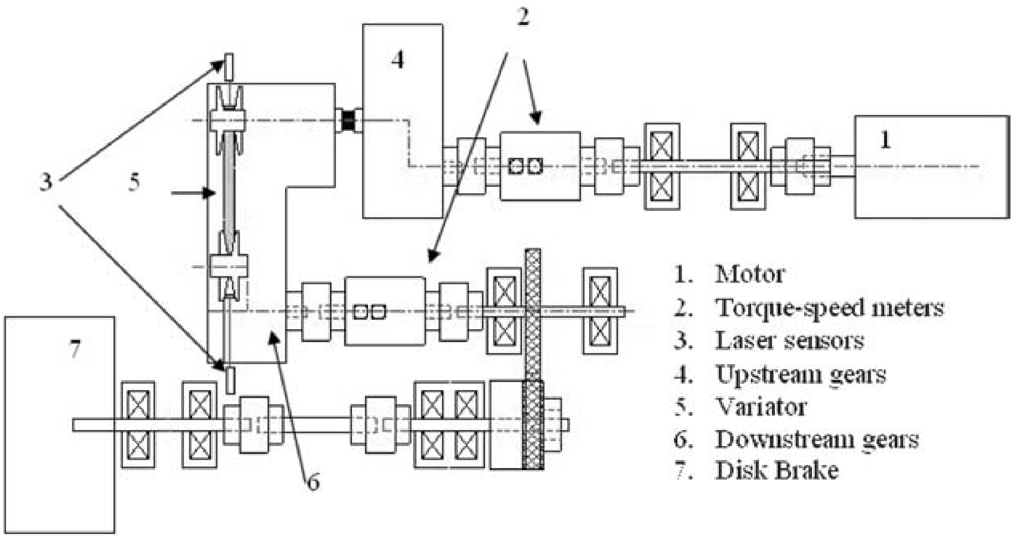

Fig. 13 Test rig

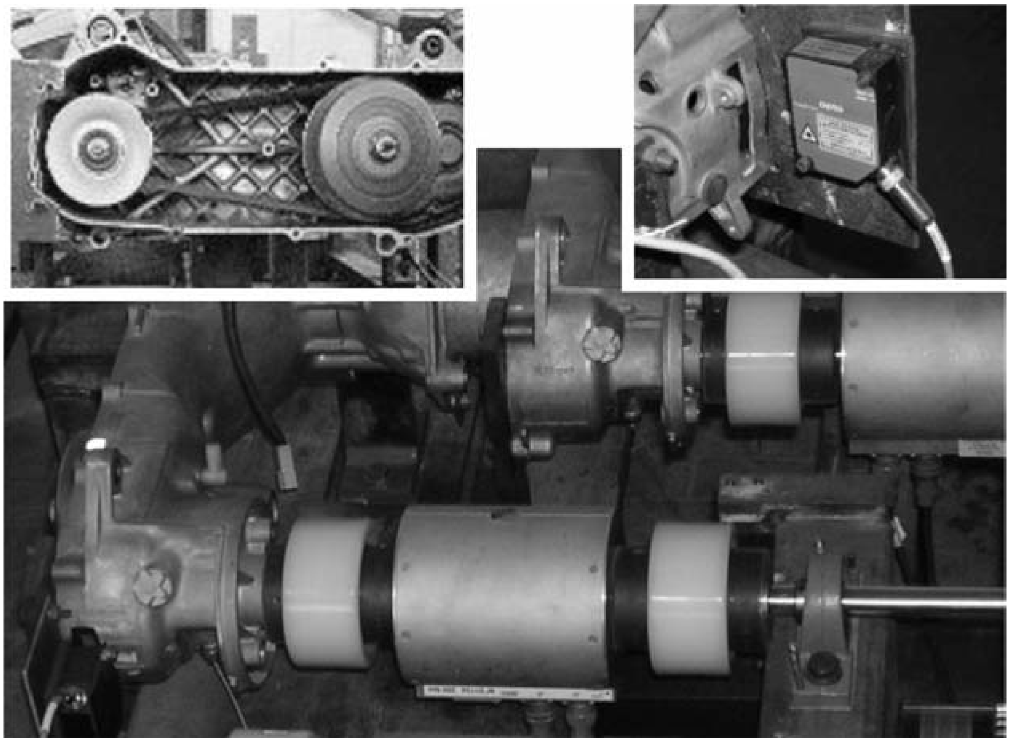

Fig. 14 Bench test particulars

the frictional forces on the roller ramps and on the sliding guides. For this reason, no frictional forces were considered in the comparisons. On the other hand, this behaviour is intrinsic in the real working of the variator.

7.4 Comparison procedure

Calculating the curved ramp slope by numerical three-point differentiation of the measured data (see Fig. 12) and using equations (13) and (14) a relationship was established between the roller centre trajectory and the wrap radius on the driver pulley. Then, by spline interpolation the functions $y_G(\tau_v)$ and $\cot \beta(\tau_v)$ were calculated.

Then, by means of equation (17) and the stored experimental data, each of the variables C_b, n_a and $\tau_v = R_a/R_b$ was calculated separately, imposing the experimental values on the other two parameters. The comparison between calculated and measured data is shown in the Figs 15 to 18, where the abscissae

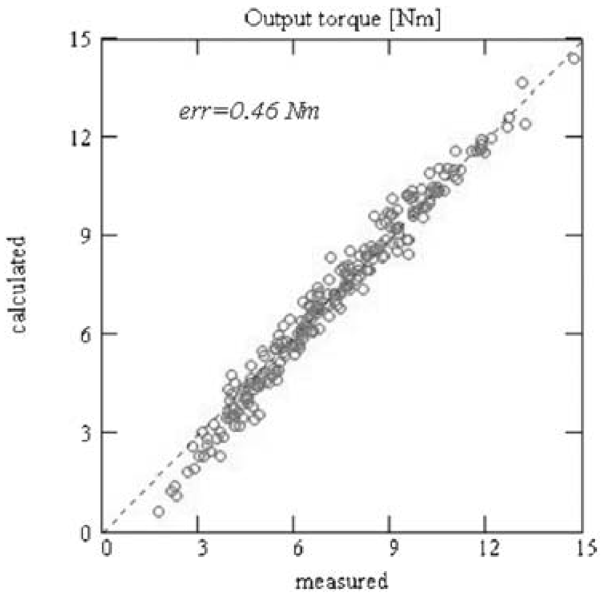

Fig. 15 Output torque comparison

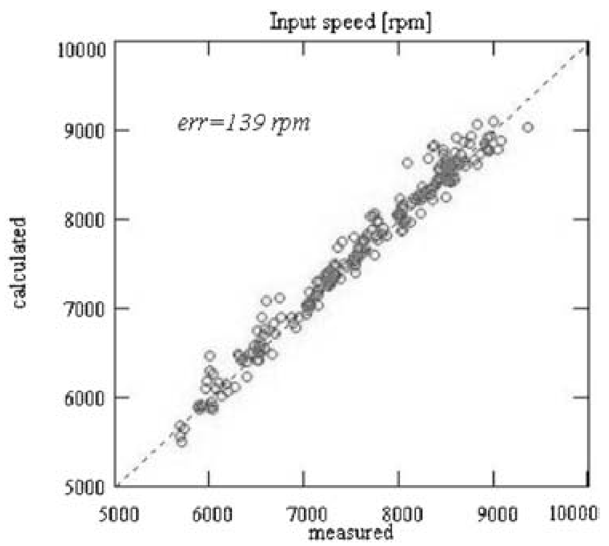

Fig. 16 Input speed comparison

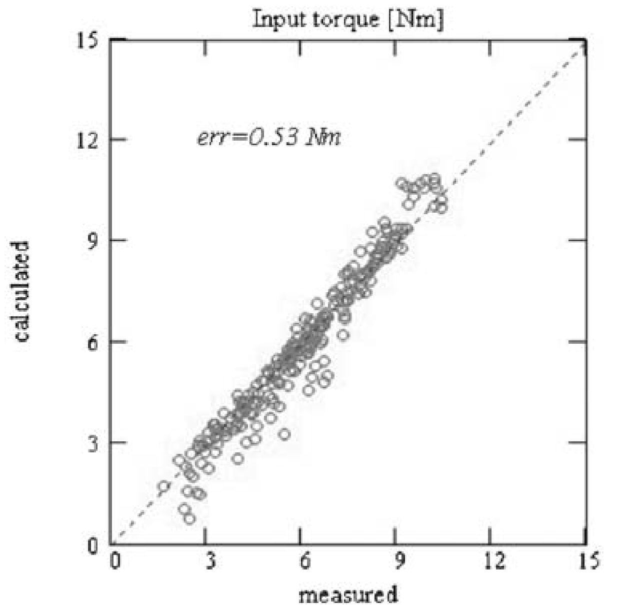

Fig. 17 Input torque comparison

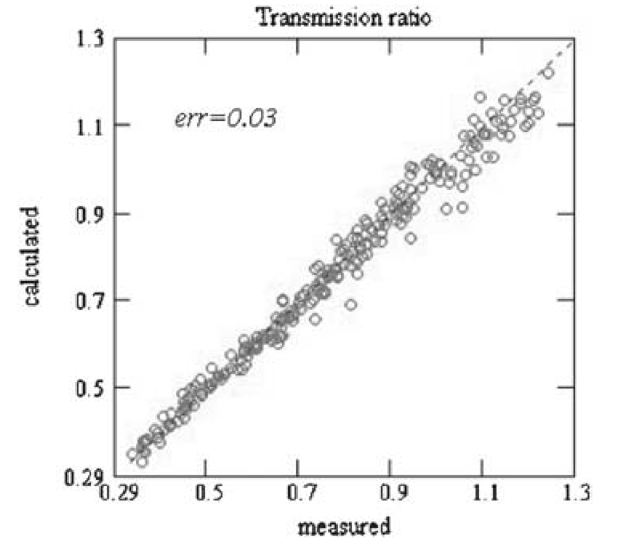

Fig. 18 Transmission ratio comparison

are measured data and the ordinates are calculated values. Moreover, each diagram reports a mean square error parameter, defined as

$$\text{error} = \sqrt{\frac{\sum(\text{calculated} - \text{measured})^2}{N}} \tag{18}$$

where $N\,(=272)$ is the number of tests. Perfect correlation would involve the condition error $= 0$, i.e. all points on the 45° dashed lines.

The correlations are considered quite good and such as to validate the analysis. The obtained results seem to be satisfactory, if the high number of tests is considered and it is kept in mind that frictional forces on the roller ramps, on the helical cam guide, and on the contact surfaces between the movable flange and the shaft have been neglected. In fact, the randomness of their direction does not permit friction to be accounted for directly.

Notwithstanding this, further tests on other variators are planned.

8 CONCLUSION

In this paper, new equations for the axial thrust of the actuators of a torque–speed-sensing rubber V-belt variator are formulated and a procedure is proposed which permits redesigning the actuator geometry in order to keep the transmissible torque as close as possible to the torque required, throughout the whole operative field.

Existing closed-form solutions for the mechanics of rubber V-belts have been used to solve the entire system of the drive equations and a correction is suggested to consider also the belt flexural stiffness.

Extensive experiments, carried out on a suitable test bench in steady state condition, validate the analysis quite well.

The proposed model is therefore an efficient tool for designing or verifying this type of transmission and offers very interesting chances as regards self-regulated split-way drives. In fact, a double-way drive imposes very different boundary conditions from the CVT unit in comparison with the simple method and different clamping forces are required from each actuator.

ACKNOWLEDGEMENT

The author acknowledges the Ministero dell' Istruzione, dell' Università e della Ricerca for financial support for this research.

REFERENCES

1 **Beccari, A.** and **Cammalleri, M.** Implicit regulation for automotive variators. *Proc. Instn Mech. Engrs, Part D: J. Automobile Engineering*, 2001, **215**(D6), 697–708.

2 **Beccari, A., Cammalleri, M.,** and **Sorge, F.** Experimental results for a two-mode split-way CVT. *VDI Ber.*, 2002, **1709**, 165–178.

3 **Oliver, L. R., Hornung, K. G., Swenson, J. E.,** and **Shapiro, H. N.** Design equations for a speed and torque controlled variable ratio V-belt transmission. SAE paper 730003, 1973.

4 **Kim, H., Lee, H., Song, H.,** and **Kim, H.** Analysis of rubber belt CVT with mechanical actuators. In Proceedings of the JSME International Conference on *Motion and Power Transmissions*, Fukuoka, Japan, 15–17 November 2001, 757–762.

5 **Sheu, K. B., Chiou, S. T., Hwang, W. M., Wang, T. S.,** and **Yan, H. S.** New automatic hybrid transmissions for motorcycles. *Proc. Natn. Sci. Coun. ROC A*, 1999, **23**(6), 716–727.

6 **Gerbert, G.** *Traction Belt Mechanics*, 1999 (Chalmers University of Technology, Göteborg).

7 **Dolan, J. P.** and **Worley, W. S.** Closed-form approximations to the solution of V-belt force and slip equations. *Trans. ASME, J. Mech. Des.*, 1995, **107**, 292–300.

8 **Miloiu, G.** Druckkraft in stufenlosen Getrieben II. *Antriebstechnik*, 1969, **8**, 450–459.

9 **Sorge, F., Beccari, A.,** and **Cammalleri, M.** Operative Variator Characterization for CVT Improvement. In Proceedings of the JSME International Conference on *Motion and Power Transmissions*, Fukuoka, Japan, 15–17 November 2001, 751–756.

10 **Sorge, F.** A qualitative–quantitative approach to V-belt mechanics. *Trans. ASME, J. Mech. Des.*, 1996, **118**, 15–21.

11 **Sorge, F.** A simple model for the axial thrust in V-belt drives. *Trans. ASME, J. Mech. Des.*, 1996, **118**, 589–592.

APPENDIX 1

Notation

C	torque
d	mean diameter of the helical guide
f	coefficient of friction of the belt–pulley
F_0	pre-load on the spring
F_z	belt axial force
F_{zact}	actuator axial force
h	pulley's centre distance
k_0	stiffness V-belt parameter (see Appendix 2)
K	spring stiffness
L	belt length
M	total roller mass
n	angular speed
q	belt mass per unit length
r	roller radius
R	winding radius
S_{f}	flexural V-belt stiffness
T_1	tight-side belt tension
T_2	slack-side belt tension
V	belt speed
x_{G}	coordinate of the roller centre
x_{P}	coordinate of the curved ramp profile
y_{G}	coordinate of the roller centre
y_{P}	coordinate of the curved ramp profile
α	groove half-angle
β	angle of the tangent to the roller centre's trajectory and the pulley axis
γ	angle of the plane ramp slope
δ	angle of the helical guide slope
Δx	axial displacement of the half-pulley
η_{s}	slip efficiency of the variator
η_{t}	torque efficiency of the variator
θ	winding angle of the belt
θ_{s}	slip angle of the belt
τ	kinematic speed ratio of the variator $= n_{\mathrm{b}}/n_{\mathrm{a}}$
τ_{v}	geometrical speed ratio of the variator $= R_{\mathrm{a}}/R_{\mathrm{b}}$
φ	angle of friction of the belt–pulley

φ_a angle of friction of the roller–ramp
φ_b angle of friction of the helical guide

Subscripts

a primary pulley
b secondary pulley
m minimum speed ratio
M maximum speed ratio
x normalized variable

APPENDIX 2

As stated in section 4.2, the analysis of the tension and the deformation of a V-belt along the contact arc on the pulley is considerably complex because of the belt elastic penetration into the groove due to the side compression of the pulley walls and the consequent radial components of the frictional forces, as will be shortly recalled hereafter.

Figure 19 shows the free body diagram of an infinitesimal V-belt element wound on the pulley. Figure 20 shows the angles defined in this appendix.

The frictional force acts on the surface of the grove. The sliding angle γ is the inclination of the frictional force with respect to the radial direction in the plane of rotation ABE (axial plane). α_s is the angle, in the sliding plane BCE, between the frictional force, directed along CE, and the plane of rotation. The wedge angle α is in the radial plane ADE (which contains also the normal contact load dF_n). CDE is the contact plane, tangent to the pulley. The angle α_s is given by the relationship $\tan\alpha_s = \tan\alpha\cos\gamma$.

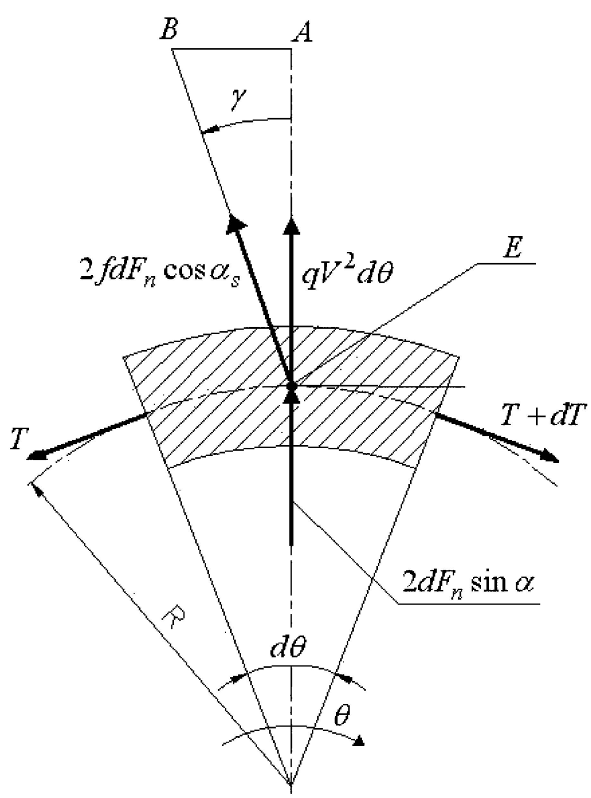

Fig. 19 Free-body diagram of an infinitesimal V-belt element

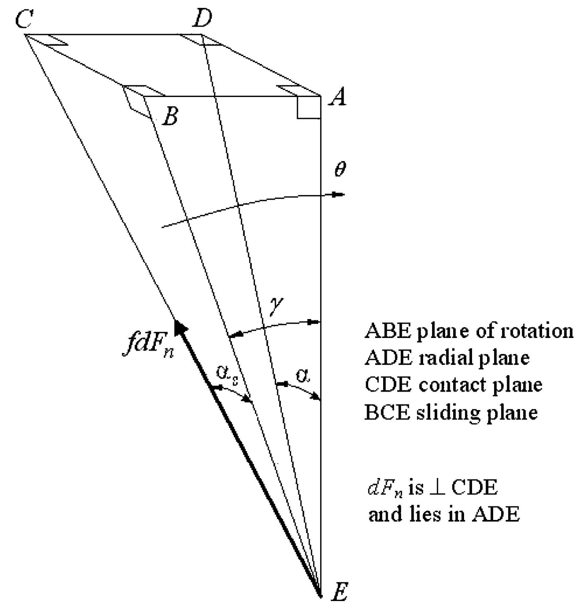

Fig. 20 V-belt angles

Equilibrium in the circumferential, radial and axial directions requires that

$$dT = 2(f\,dF_n\cos\alpha_s)\sin\gamma$$

$$2T\frac{d\theta}{2} = 2\,dF_n\sin\alpha + qV^2\,d\theta + 2(f\,dF_n\cos\alpha_s)\cos\gamma$$

$$dF_z = dF_n\cos\alpha - f\,dF_n\sin\alpha_s$$

and hence

$$\frac{dT}{T - qV^2} = f'\,d\theta$$

where

$$f' = \frac{f\cos\alpha_s\sin\gamma}{\sin\alpha + f\cos\alpha_s\cos\gamma}$$

and also

$$dF_z = \frac{1}{2}\,\frac{\cos\alpha - f\sin\alpha_s}{\sin\alpha + f\cos\alpha_s\cos\gamma}(T - qV^2)\,d\theta$$

f' can be considered as a fictitious coefficient of friction ($\gamma = \pm 90^\circ$ leads to the Euler–Grashof model without penetration).

Along the idle arc, the static frictional force direction remains radial like at the entrance ($\gamma = 0^\circ$)

and the longitudinal tension remains constant (as $\alpha_s = \alpha$, $dF_z = (T - qV^2)/[2\tan(\alpha+\varphi)]$; this explains the presence of $\tan(\alpha+\varphi)$ in equations (3) and (4)). Along the sliding arc, on the contrary, the longitudinal tension changes and γ is variable. In fact, the change in the transverse elastic deformation makes the belt move radially into the pulley groove, producing radial components of the slip velocity and the frictional force. The above equations can no longer be integrated directly in order to obtain the functions $G(\theta_s, \tau_v)$ and $Z(\theta_s, \tau_v)$ of section 4.2.

Moreover, as γ and the sliding direction are unknown functions of θ, the calculation of the longitudinal elastic deformation and the radial penetration of the belt along the whole contact arc requires the formulation of other conditions, such as the belt constitutive equation and the mass conservation condition. This leads to a non-linear differential system of the third order, which can be solved only by numerical integration (e.g. Runge–Kutta) [**6**, **10**]. Reference [**9**] (see also reference [**11**]) shows that, for belts much stiffer in the longitudinal direction than in the transverse direction, the numerical solutions can be suitably interpolated by approximate closed-form solutions. Figure 21, which shows the longitudinal deformation $\varepsilon/\varepsilon_0$ and radial penetration x/x_0 versus slip angle θ_s, gives a comparison between the approximate analytical solutions and the numerical solutions.

These approximate solutions allow

$$G_b(\theta_{sb}, \tau_v) = 1 + \frac{p}{2k_1}\frac{k_1 - k_2}{p - k_2}[\cosh(\Omega\theta_{sb}) - 1]$$

$$Z_a(\theta_{sa}, \tau_v) \approx \theta_a$$

$$Z_b(\theta_{sb}, \tau_v) = \theta_b + \frac{k_1 - k_2}{p - k_2}\frac{1}{2}\left[\frac{\sinh(\Omega\theta_{sb})}{\Omega} - \theta_{sb}\right]$$

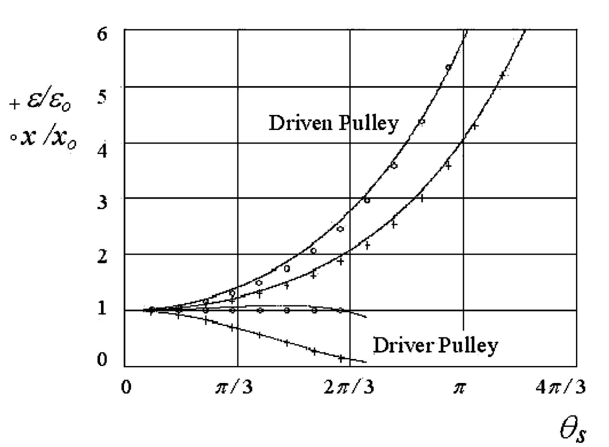

Fig. 21 Comparison between approximate closed-form and numerical solutions for the V-belt

where k_1, k_2, p and Ω are parameters dependent on the speed ratio τ_v and the belt stiffness, to be obtained.

Putting $k = 2\tan\alpha S_\perp/S_\parallel$, where $S_\perp$ and $S_\parallel$ indicate the transverse and longitudinal stiffnesses respectively of the belt [**10**], results in $k_1 = k\tan(\alpha+\varphi)/\tan\alpha$, $k_2 = k\tan(\alpha-\varphi)/\tan\alpha$. Since $S_\perp = EsR_b^2/H$, where E = Young's modulus of the rubber (see Fig. 22 regarding s and H), it is found that k is proportional to R_b^2 and, thus, is dependent on the speed ratio. Indicating the value of k for $\tau_v = 1$ as k_0 gives $k = k_0(R_b/R_{b1:1})^2$. Moreover, the best fit is obtained if the number p is given by $p = 0.6\,p_0 + 0.4\,p_\infty$, where

$$p_0 = \sqrt{(1.5 - f\tan\alpha)^2 + 2k\left(1 + \frac{f}{\tan\alpha}\right)} - (1.5 - f\tan\alpha)$$

and p_∞ is the largest real root of the cubic equation in w, namely

$$w^3 + (2 - k - f^2\tan\alpha^2)w^2 - (3 + 2f^2)kw + k^2\left[1 - \left(\frac{f}{\tan\alpha}\right)^2\right] = 0$$

Finally,

$$\Omega = \frac{\sqrt{(k_1 - p)(p - k_2)}}{p}\,\frac{\sqrt{\cos(\alpha+\varphi)\cos(\alpha-\varphi)}}{\cos\varphi}$$

For $k_0 \leqslant 0.15$, the results obtainable by these approximate solutions are very close to the numerical

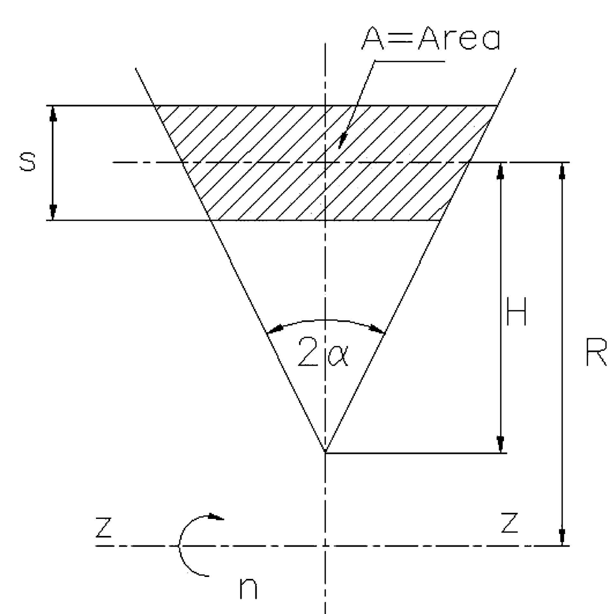

Fig. 22 V-belt cross-section

solutions. The value of k_0 can be obtained experimentally as described in reference [**9**].

APPENDIX 3

The flexural stiffness of the belt can be obtained by suspending it as in Fig. 23 and measuring the downward displacement w of the bottom point due to the weight $Q = Lqg$ ($g =$ acceleration of gravity). Indicating with N and M the internal axial load and bending moment on the top cross-section, where the shear force is $Q/2$, and neglecting the belt elongation, the deflection equation is:

$$\frac{d^2\phi}{d\vartheta^2} - \frac{NR_0^2}{S_f}\sin(\vartheta + \phi) + \frac{QR_0^2}{2S_f}\left(1 - \frac{\vartheta}{\pi}\right)\cos(\vartheta + \phi) = 0$$

where $\vartheta = 2\pi s/L$ is a dimensionless curvilinear coordinate along the belt and ϕ is the rotation of the generic belt element with respect to the unloaded circular shape of radius R_0. The coordinates of the belt line can be obtained by integration of $dx = R_0 d\vartheta \sin(\vartheta + \phi)$ and $dy = R_0 d\vartheta \cos(\vartheta + \phi)$. Four boundary conditions must be imposed: $\phi = 0$, $d\phi/d\vartheta = R_0 M/S_f$ for $\vartheta = 0$ and $\phi = y = 0$ for $\vartheta = \pi$. They are consistent with the number of unknowns: N, M and two integration constants. The deflection was calculated by an iterative shooting technique, changing N and M until the final boundary conditions, $\phi = y = 0$ for $\vartheta = \pi$, were fulfilled. Comparing with the experimental tests, the number $S_f \cong 10\,000$ N mm^2 was at last evaluated.

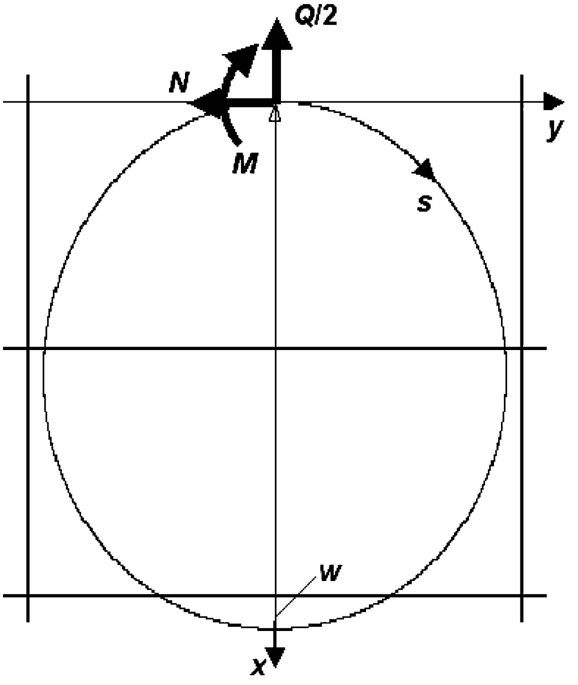

Fig. 23 Hanging belt